

# Influence of Disorder and Finite-Size Effects on Slow Light Transport in Extended Photonic Crystal Coupled-Cavity Waveguides

Mohamed Sabry Mohamed,<sup>\*,†,‡</sup> Yiming Lai,<sup>‡,§</sup> Momchil Minkov,<sup>||</sup> Vincenzo Savona,<sup>†</sup> Antonio Badolato,<sup>‡,§</sup> and Romuald Houdré<sup>†</sup>

<sup>†</sup>Institute of Physics, Ecole Polytechnique Fédérale de Lausanne (EPFL), Lausanne 1015, Switzerland

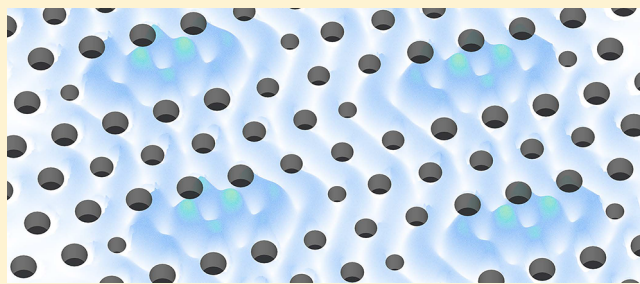
<sup>‡</sup>Department of Physics, University of Ottawa, Ottawa, Ontario K1N 6NS, Canada

<sup>§</sup>Center for Nanoscale Science and Technology, National Institute of Standards and Technology, Gaithersburg, Maryland 20899, United States

<sup>||</sup>Ginzton Laboratory, Stanford University, Stanford, California 94305, United States

**ABSTRACT:** A convenient approach for slowing down light in integrated optical circuits is by utilizing a set of coupled microcavities in a photonic crystal lattice. While this provides for flexibility in dispersion engineering, light transport is influenced by a combination of disorder and finite-size effects, setting limitations on the achievable slow light properties. In this study, the experimental characterization of slow light photonic crystal waveguides based on a coupled-cavity design is presented in the near-infrared wavelength range for extended chains comprising up to 800 cavities. The dispersive behavior of light along the waveguides is probed through Fourier-space imaging to elucidate the influence of disorder and cavity chain length on the optical response of the implemented design. Constraints on the slow-down factor of Bloch modes are identified in terms of decay length and induced light localization.

**KEYWORDS:** Photonic crystals, slow light, coupled-cavity waveguides, disorder



Over the past two decades, rapid development in the field of slow light has been triggered by the pursuit of novel, high-performance optical devices. The interest in an integrated and controllable slow light system stems from the necessity of on-chip buffering of optical signals, whether for classical light or fragile quantum states. Additionally, slow light offers a mechanism for enhancing light-matter interaction, whereby the electromagnetic energy density within a material can be elevated according to the slow-down factor. A wide range of applications in integrated optical circuits can benefit from slow light, among which include the following: interferometry,<sup>1,2</sup> generation of nonclassical light,<sup>3,4</sup> and the synchronization of emitters in quantum networks.<sup>5</sup>

Photonic crystal (PhC) lattices present an ideal platform for generating slow light as they allow for synthesizing the optical response in the material of choice. In comparison to a material resonance-based approach, the slow light effect emerges from a wavelength-scale rather than a smaller atomic-scale interaction. PhCs however have the merit of being scale-invariant, and consequently, the operational wavelength can be readily set by design. Moreover, slow light in PhCs is achievable over a bandwidth that is a few orders of magnitude larger, added to the relative freedom in dispersion engineering which is crucial for any application that envisions pulse propagation. The

overall compactness of PhC designs makes them ideally suited for integrated optical circuits.

Slow light implementations in PhCs have—for the most part—relied on designs based on either line-defect (W1) waveguides or coupled-cavity waveguides (CCW). Coupled-cavity systems are distinct by their nature of state hybridization, which mimics molecular bonding, and they are therefore commonly referred to as photonic molecules. The optical response of CCWs can be modeled in an analogous manner through a tight-binding formulation. Implementations of CCW slow light have so far demonstrated successful coupling between cavity chains extending beyond 100 cavities in length.<sup>6–9</sup> We have recently developed optimized silicon CCW devices, achieving record-high group index-bandwidth product values for slow light, as large as 0.47.<sup>8,10</sup> The CCW design offers broadband operation yet with increased losses compared to previous implementations.<sup>11</sup> PhC coupled-cavity chains comprising up to 800 cavities have been successfully realized, which exceed 500  $\mu\text{m}$  in length.

Depending on the targeted application, it may be desirable to elongate CCWs whether to prolong the signal delay time or to expand the effective light-matter interaction volume. With

Received: July 13, 2018

Published: November 12, 2018

the implementation of extended coupled-cavity chains, however, several effects contribute to the deterioration of the optical response. In this study, we experimentally investigate limitations imposed on slow light transport in extended CCW structures considering state-of-the-art fabrication. With the aid of Fourier-space imaging, features emerging due to fabrication-induced disorder as well as those due to the finite size of the structures are highlighted, and the impact on the optical response and device performance is clarified.

## SAMPLE DESIGN

The implemented CCW design relies on a staggered arrangement of modified L3 cavities in a Si membrane, which utilizes a two-barrier evanescent coupling configuration for dispersion control,<sup>10</sup> as shown in Figure 1. The first- and

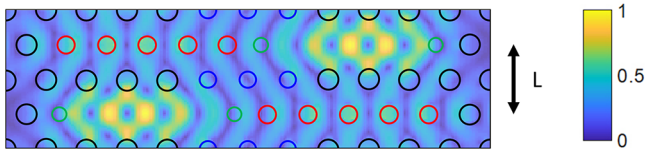


**Figure 1.** Schematic illustration of the coupled-cavity waveguide unit cell and the normalized field intensity of the fundamental mode near the center of the bandwidth. The tunable first- and second-neighbor PhC barrier holes are indicated in blue and red, respectively, while the L3 cavity side holes utilized for the optimization of radiative losses are shown in green.

second-neighbor cavity-coupling strengths are adjusted by altering the PhC hole size at the respective barrier site. The CCW operates near  $\lambda = 1550$  nm and improves on previous slow light implementations with respect to the optimization of the group index ( $n_g$ )-bandwidth product ( $\text{GBP} = n_g \Delta\omega/\omega$ ). The compact alignment of the cavities along the  $\Gamma\text{M}$  direction of the PhC lattice yields an effective periodicity of  $L = a\sqrt{3}$ , where  $a$  is the PhC lattice constant. This maximizes the momentum span of the waveguide unit cell, thereby expanding the operational bandwidth. A center  $n_g$  value of 37 is obtained over a bandwidth of 18.0 nm, the latter which is defined in terms of the 10% deviation range from the center  $n_g$  value (rather than the 3-dB attenuation limit). This is deemed a more relevant criterion for slow light devices, especially for pulse propagation.

The optimization further accounts for the reduction of radiative losses by controlling the size and position of the inner holes of the L3 cavity such that loss value within the operational bandwidth does not exceed 100 dB/ns. Apodization, i.e. a windowing function applied to the cavity-coupling strength distribution,<sup>12</sup> has not been considered for the CCW terminations due to the fabrication tolerance that is required in PhCs for coupling control. The CCW is interfaced at both ends by W1 waveguides, which are preceded by tapered Si wire waveguides and SU8 spot-size converters toward the sample facets. Sample fabrication was carried out using state-of-the-art tools, for which the process details can be found in the Methods section. Stress-releasing nanobeam support structures were incorporated in the design to prevent Si membrane buckling and maintain optical uniformity along the entire device.<sup>13</sup>

## EXTRACTION OF SLOW LIGHT PROPERTIES

Dispersion maps of the CCW modes were acquired through Fourier-space imaging reconstruction,<sup>14</sup> to help extract the slow light properties. More information on the experimental technique can be found in the Methods section. Figure 2(a)

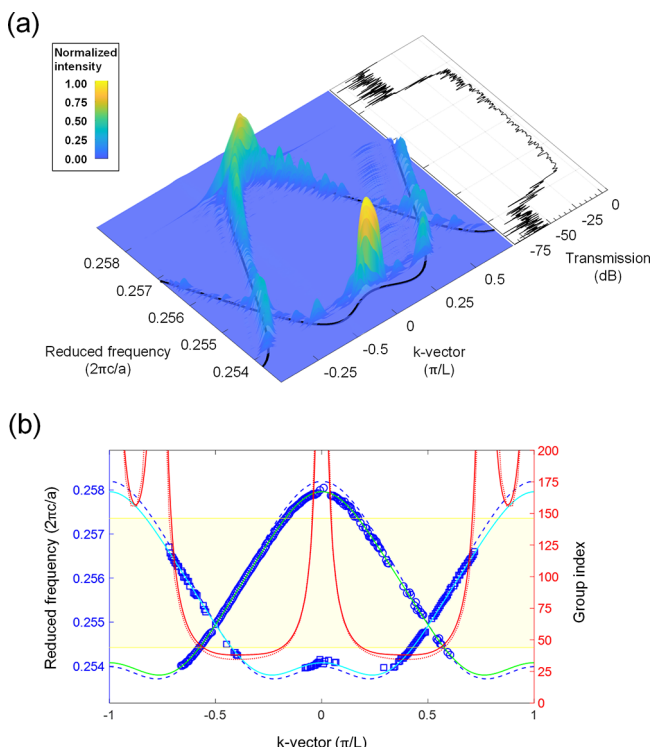


**Figure 2.** (a) Experimental dispersion of a 200-cavity CCW, obtained through Fourier-space imaging reconstruction, with the GME-computed dispersion curve overlaid in black. The simultaneously acquired transmission spectrum is displayed alongside. (b) The experimental dispersion points (blue circles/squares), extracted from the Fourier-space imaging acquisition, and tight-binding fit (green/cyan line) for the diffraction orders of the CCW modes, along with the GME-computed dispersion (dashed blue line) for comparison. The group index of a single diffraction order (blue circles) is plotted for: derivation from the tight-binding fit (solid red line) and derivation from the theoretical GME dispersion (dotted red line). The operational bandwidth is highlighted in yellow.

displays the dispersion acquisition from a CCW comprising 200 cavities, along with the simultaneously acquired transmission spectrum. Individual states of the supported CCW mode are visible, outlining a quasi-continuous dispersion relation that is found to closely match the theoretical dispersion predicted by guided-mode expansion (GME) computations. The experimental Brillouin zone boundary is well-defined in k-space, following from the near-nanometer accuracy of the structural patterning by electron-beam lithography. Although the excitation scheme favors injection into the forward propagation direction, both forward and backward propagating modes of the CCW appear in the acquired dispersion. This is due to the induced coupling between them via multiple scattering events, which increase in magnitude as the group index of the mode rises. The modes can be seen mirrored about the  $k = \pm\pi/2L$  axes and exhibit a folding period of  $k = \pi/L$ , corresponding to the extended Brillouin zone boundary. The forward propagating mode

$(\frac{d\omega}{dk} > 0)$  is found to dominate the operational bandwidth, as deduced by the measured intensity since the CCW modes are intrinsically radiative.

The transmission measurement clearly outlines the operational range of the device and validates the obtained dispersion. It should be noted that the transmission does not showcase the pure CCW response but rather incorporates the modulation introduced by the various interfaces, including the frequency-dependent coupling at the CCW-W1 junction. At the origin of the fluctuation in transmission intensity is the overlap of the finite constituent states of the CCW, while fluctuations of higher amplitude near the edge of the bandwidth are caused by interference effects due to the absence of apodization. CCW terminations act effectively as mirrors due to the diminishing CCW-W1 coupling rate when  $n_g$  rises. The transmission is additionally impacted by disorder-induced effects such as multiple scattering, which scale with the slow-down factor, and whose contribution becomes increasingly prominent as the CCW chain is elongated.

State sampling of the CCW mode is carried out via frequency weighing of the radiative intensity to extract the dispersion points. The retrieved dispersion function  $\omega(k)$  is discretized by the k-space resolution of the acquisition, as displayed in Figure 2(b). Since this technique relies primarily on intrinsic mode radiation, the dispersion curve is well-defined for the case of the forward propagating mode, where the energy is coupled. A direct measure of the group index can be obtained through numerical differentiation of the dispersion points. By further applying a tight-binding model fit that accounts additionally for second-neighbor coupling terms,<sup>15</sup> the group index is computed with higher accuracy, yielding an uncertainty below 1% within the operational bandwidth. For the shown 200-cavity CCW, an average group index of 41.7 is achieved over a bandwidth of 17.4 nm, equating to a GBP value of 0.47. The experimental bandwidth is found to be marginally narrower compared to theory, which is attributed to slight deviations in the cavity resonance frequency and intercavity coupling strength due to limitations on the control of PhC hole diameter with the etch process. This implies that for the same Brillouin zone extent the dispersion lines are less steep, exhibiting slightly slower light as a result, which is indeed what is attained here.

## ■ OPTICAL RESPONSE: FEATURES EMERGING DUE TO FINITE-SIZE EFFECTS AND DISORDER

There is a fundamental discretization of states in the dispersion response of CCWs due to the finite size of the implemented structures, in contrast to theoretical formulation which assumes periodic boundaries. Since the CCW design under investigation features a broad bandwidth, spanning a frequency range up to 3 orders of magnitude the size of the natural line width of the elemental states, state discretization becomes evident especially in cavity chains comprising fewer than  $10^3$  cavities. According to a tight-binding description, N states are expected to be observed for an N-cavity system. Individual peaks are discernible in the acquired experimental dispersion, particularly near the edge of the band where state line width narrowing occurs and radiative scattering losses are intrinsically higher.

Achieving continuous dispersion relies fundamentally on the ability to occupy the dispersion curve with overlapping propagative states. The required number of states can be

derived from the continuity conditions with respect to both momentum and frequency. For a system of N coupled optical resonators and cavity periodicity of  $\Lambda$ , state separation in momentum can be estimated to be  $\Delta k = \frac{\pi}{(N+1)\Lambda}$ . This is according to a tight-binding model, provided truncated boundaries, while the momentum spread of each state due to the finite sample size is given by  $\delta k \geq \frac{2\pi}{(N-1)\Lambda}$ , with additional broadening introduced by mode attenuation.<sup>16</sup> Thus, continuity in momentum is consistently fulfilled. Continuity in frequency, on the other hand, is attained when the state line width  $\delta\omega$  exceeds the state separation  $\Delta\omega = \frac{c}{n_g}\Delta k$ , which can be summed up by the following condition on the number of states:  $N + 1 \geq \frac{1}{\delta\omega n_g} \frac{c}{\pi} \frac{\pi}{\Lambda}$ . The dispersion profile is expected to gradually coalesce when the cavity chain is elongated, as the interstate frequency gaps narrow down with the inclusion of additional states. While the fabricated 800-cavity CCW of the considered design still falls short of fulfilling this criterion, which necessitates  $N > 1.4 \times 10^3$ , CCWs on this length scale are already highly susceptible to disorder. It should be noted that this requirement on N applies to the considered CCW parameters ( $n_g = 41.7$  and  $\delta\omega = 2\pi \times 3.7$  GHz). Alternatively, one can rely on CCW designs that incorporate cavities of intrinsically shorter lifetime to partially alleviate the condition on chain length.

A comparison between the experimental dispersion profiles of the forward propagating mode near the edge of the dispersion band for CCWs of varying length is displayed in Figure 3, through which the state lifetimes were analyzed. The dispersion was acquired spatially at the beginning of the CCWs, adjacent to the CCW-W1 coupling point to capture the full dispersion band, including non-propagative states. The dispersion curves of the devices were aligned by referencing the frequency axis to the  $k = \pi/2L$  dispersion point frequency ( $\nu_0$ ), which is equal to 0.2558, 0.2549, and 0.2550 for the 50-, 200-, and 800-cavity CCW, respectively. The state Q-factor values were extracted through collective Lorentzian profile fitting to the radiative intensity. It is evident that as the number of coupled cavities in the waveguide increases, the state population density grows in direct proportion, while the individual states exhibit reduced spectral broadening. The latter effect is a consequence of the increase of the coupled-cavity state lifetime as the CCW response in longer chains progressively transitions toward the intrinsic periodic-boundary value, where theoretical Q-factor values of the modes vary between  $\approx 0.25 - 1.94 \times 10^5$  for the displayed frequency range. Theoretical Q-factor values are obtained from three-dimensional FDTD simulations by assessing the field decay time within a CCW unit cell, under periodic boundary conditions with preset Bloch momentum vectors. The primary contribution toward the reduced spectral broadening of CCW states comes from the reduced coupling to the W1 waveguide as the CCW is elongated, such that the coupled-cavity states exhibit a decay rate that is closer to their natural line width. Furthermore, an expected rise in state Q-factors with increasing  $n_g$  toward the edge of the band is observed for all CCW lengths.

It is expected that the optical response of a CCW would converge to that of the theoretical Bloch-boundary device as the CCW chain is extended, as seen with the evolution of the state lifetimes. Analysis of the experimental first-neighbor

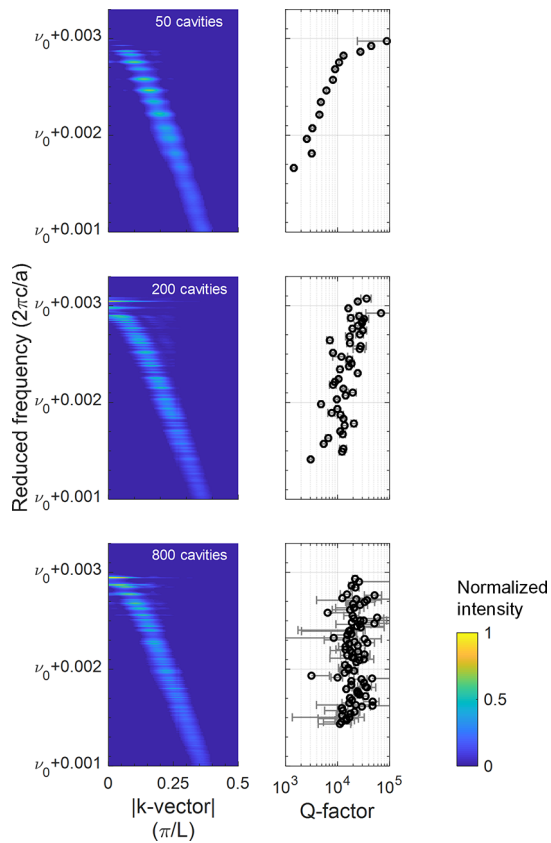


**Figure 3.** Experimentally acquired dispersion for a 50-, 200-, and 800-cavity CCW, displaying the intensity of the forward propagating mode, and the corresponding Q-factors (95% confidence interval in gray) of the states near the edge of the band.

coupling strength additionally confirms the convergence, as frequency-normalized values of  $[7.88 \ 7.97 \ 8.04] \pm 0.03 \times 10^{-3}$  are extracted for the [50 200 800]-cavity CCWs. This is to be compared to a theoretical value of  $8.70 \times 10^{-3}$  from the GME computation.

However, fabrication-induced disorder in the PhC lattice can severely limit the optical performance in longer waveguides. This is particularly apparent when assessing the transmission band of the devices. The flatness of the transmission was found to degrade in terms of the appearance of intensity fluctuations of increasing contrast and higher frequency density as the devices were elongated, as displayed in Figure 4(a) for a  $\Delta\lambda = 10$  nm range around the center of the bandwidth. It has been proposed through a simplified disorder model<sup>17</sup> that such dips in transmission emerge due to disorder-induced loss and scattering events. The disorder figure of the sample  $\sigma_{disorder}$  which indicates the magnitude of random fluctuation in either hole position or radius along a single spatial direction, was determined to be 0.6 nm, based on previous statistical analysis of isolated PhC cavity Q-factors in similar fabrication runs.<sup>18</sup> An exponential dependence of the RMS transmission fluctuation on the CCW length is deduced from the plot in Figure 4(b). It is measured on average to be  $4.9 \times 10^{-3}$  dB/cavity across the bandwidth and  $1.9 \times 10^{-3}$  dB/cavity for a  $\Delta\lambda = 1$  nm window near the center of the transmission band.

A gradual contraction in the size of the transmission band occurs with increasing device length as well. In the presence of disorder-induced scattering, the  $n_g$ -dependent decay length imposes a limit on the transmitted group index values,

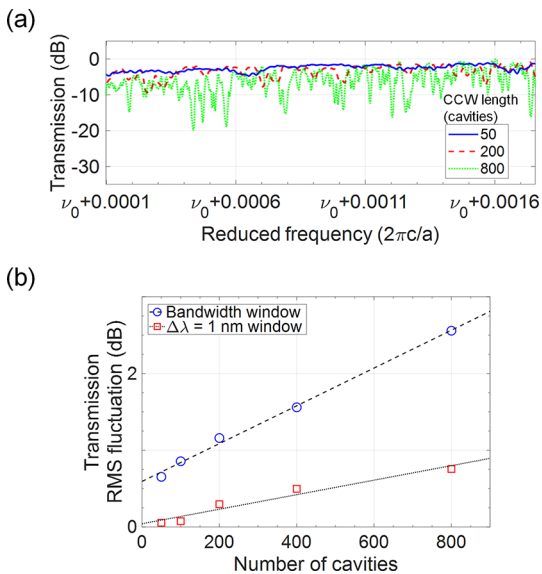


**Figure 4.** (a) Transmission across a 10 nm-wavelength range around the center of the bandwidth for each of the CCW devices. (b) RMS fluctuation of the transmission as a function of CCW length, measured across the operational bandwidth (blue circles) and across a 1 nm-wavelength window (red squares).

according to the device size. The decay in transmission however lies primarily outside the operational bandwidth for CCW length up to 400 cavities.

We have verified this effect through tight-binding model analysis. The nominal design parameters were simulated: center frequency ( $\nu_c$ ) = 0.2554, intrinsic cavity Q-factor =  $10^5$ , and frequency-normalized first- and second-neighbor coupling strength  $g_1' = 8 \times 10^{-3}$  and  $g_2' = 2 \times 10^{-3}$ , respectively. An order-of-magnitude estimate was considered for the cavity Q-factor, while the coupling strength values were obtained from a tight-binding fit to the GME-computed dispersion curve. Disorder was accounted for by introducing random shifts in the cavity resonance frequencies and coupling strength values through a statistical Gaussian distribution of zero mean. The standard deviation of the resonance frequency distribution ( $\sigma_\nu$ ) was set to  $3 \times 10^{-4} \nu_c$ , in line with the experimental statistics of resonance frequencies in isolated cavities, for similar fabrication runs.<sup>18</sup> As for the coupling strength values  $g_1'$  and  $g_2'$ , the standard deviations of their distribution ( $\sigma_{g_{1,2}'}$ ) were set to  $5 \times 10^{-3} g_{1,2}'$ , which is an appropriate estimate following the analysis in ref 19, when accounting for the aforementioned disorder figure. The inverse participation number (IPN), defined as the second moment of the probability density function,<sup>20</sup> quantifies the spatial extent of a localized mode.<sup>21</sup> The localization length was computed using the IPN through  $[\int |\varphi(x)|^4 dx]^{-1}$ , where  $\varphi(x)$  is the state wave function (normalized to unity). The results, displayed in Figure 5(a) for varying CCW length, support the experimentally observed trends with respect to transmission band size and intensity fluctuations. Near the center of the transmission band, the localization length (expressed in number of cavities) is naturally bound by the device size when not limited by disorder. With increasing CCW length, the localization length tends to diminish earlier toward the band edge, and localized states emerge across the band causing dips in transmission. The magnitude of disorder present in the coupling strength

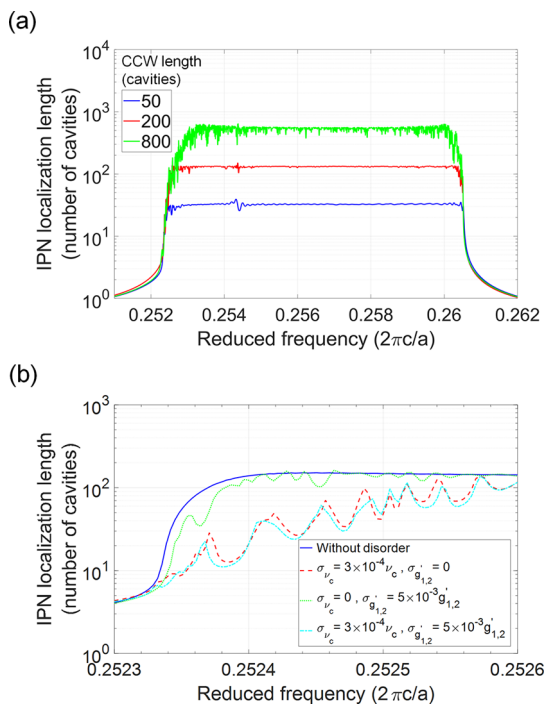


**Figure 5.** (a) Localization length for varying CCW size, computed through the inverse participation number based on a tight-binding model which incorporates random disorder ( $\sigma_{\text{disorder}} = 0.0015a$ ) impacting both cavity resonance frequency and coupling strength. (b) Computed localization length for a 200-cavity CCW near the low-frequency edge for different disorder configurations: without disorder (blue), disorder in  $\nu_c$  only (red), disorder in  $g_{1,2}$  only (green), and disorder in both  $\nu_c$  and  $g_{1,2}$  (cyan).

however was found to have far less impact on transmission fluctuations in comparison to that of the cavity resonance frequencies. This can be seen through the computed localization length in Figure 5(b), when analyzing each contribution of disorder separately.

## ■ ATTENUATION, DIFFUSIVE LIGHT TRANSPORT, AND THE TRANSITION TOWARD LOCALIZATION

Beyond the CCW-W1 interface, light does not naturally couple to backward propagating modes unless mediated by an elastic scattering process. A measure of the backscattered signal therefore acts as a gauge for the degree of disorder and the density of defects in the medium. Figure 6 displays the backward propagating mode dispersion near the high-frequency edge of the band, for a range of CCW lengths. The intensity is normalized relative to that of the forward propagating mode, and the  $x$ -axis displays the magnitude of the momentum vector. When the CCW chain length is relatively short, up to 100 cavities, backscattering appears only at high  $n_g$  values exceeding  $\approx 65$ , which exist outside the operational bandwidth. This however does not hold for longer CCWs, as coupling to backward propagating modes gradually extends to lower  $n_g$  values lying within the bandwidth due to multiple scattering events. Considering the disorder figure associated with the fabrication, the average localization length based on the simulated tight-binding model is estimated to be  $\approx 865 \mu\text{m}$  (equivalent to  $\approx 1250$  cavities) near the center frequency. As the CCW chain length becomes comparable to this value, light becomes more prone to dephasing, and scattering into the backward propagating mode intensifies at a given  $n_g$  value.

The scattering contribution due to disorder in a medium is elevated by the slow-down factor, which in this case provides undesirable enhancement of light-matter interaction. The reduction of the mean free path toward the band edge implies that light enters a diffusive transport regime, manifested in the induced momentum broadening of the mode. The dispersion becomes loosely defined from this point onward. A gradual rise in the intensity of the backscattered signal is observed along the dispersion curve as a function of  $n_g$ , up to the point where it becomes comparable to that of the forward propagating mode, near the localization limit of light. This ultimately restricts the lowest achievable group velocity in any device.

It is known that radiative losses into the continuum go according to the density of states, which should naturally scale

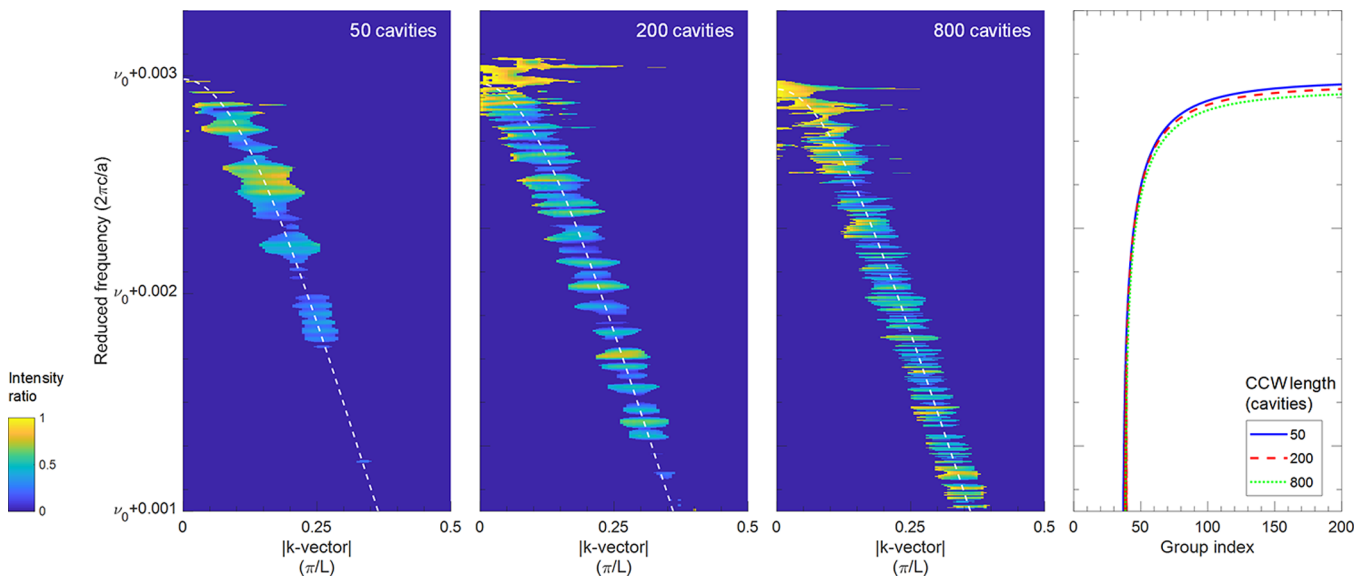


**Figure 6.** Acquired experimental dispersion of the backward propagating mode for a 50-, 200-, and 800-cavity CCW. The intensity is normalized relative to the forward propagating mode, and the experimental tight-binding dispersion fit is overlaid (dashed white line). The corresponding extracted group index value dependence is plotted alongside.

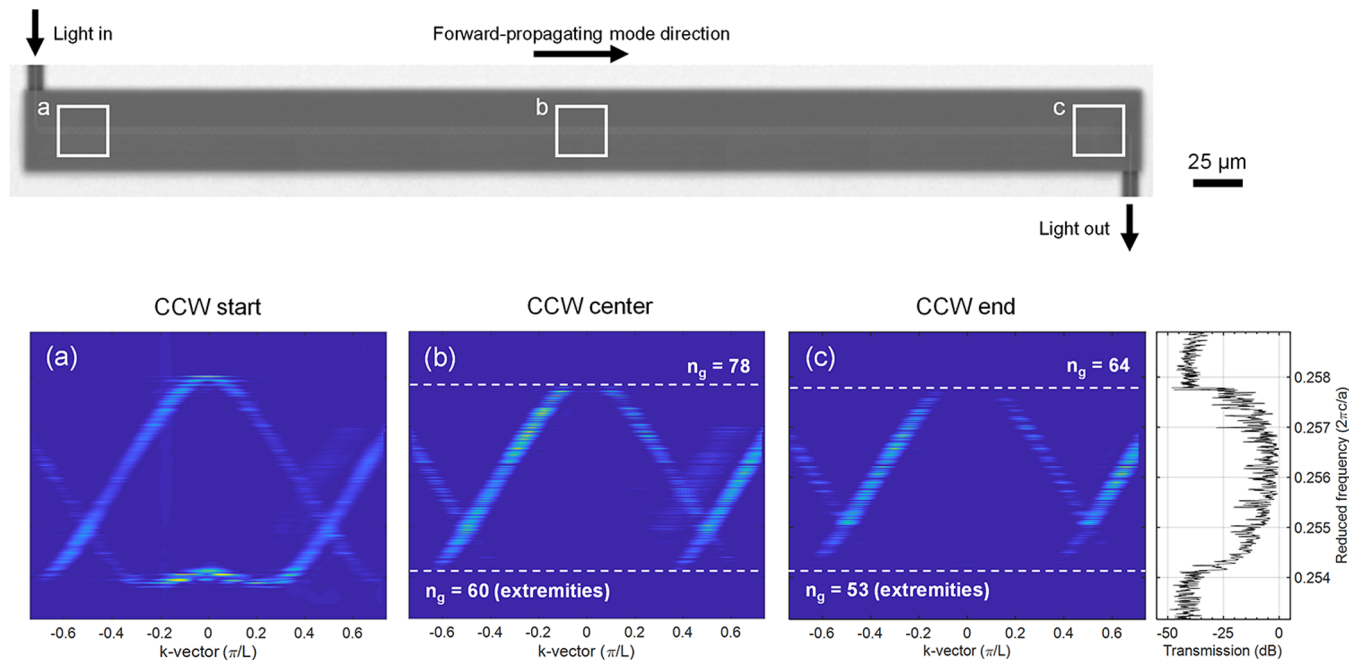


**Figure 7.** Experimental dispersion acquired from an 800-cavity CCW at the (a) start, (b) center, and (c) end of the CCW (as outlined in the schematic above), along with the transmission. The cutoff group index value is indicated by the dashed white line.

with  $n_g$ . It has been suggested by Hughes et al.<sup>22</sup> that for backscattering, the scaling goes according to  $n_g^2$ , an estimate based on a second-order Born approximation. It accounts additionally for the density of states of the backward propagating modes. Near the high-frequency edge of the band, the scattering intensity was measured to have an exponential dependence of 1.2 and 2.4 on  $n_g$  for the forward and backward propagating modes, respectively, considering the 800-cavity CCW. The  $n_g$  power scaling here is found to be slightly above the aforementioned theoretical values, which is expected in the presence of disorder.<sup>23</sup> Deviations in the frequency dependence of scattering originate from the varying Bloch mode profiles that sample disorder differently, as well as the frequency-dependent nature of light-cone radiative losses. Forward and backward propagating modes however maintained a scattering  $n_g$ -dependence exponential ratio of 1:2 for all device lengths.

The  $n_g$ -dependent attenuation of light was analyzed through the dispersion of an 800-cavity CCW, acquired at the beginning, center, and end of the device. The results are displayed in Figure 7. Near the input, the entire dispersion curve of the CCW is reconstructed, with localized states appearing as well, but only within a distance of a few microns specified by their decay length. Near the center of the CCW, the  $n_g$  propagation limit at the high-frequency end of the dispersion is found to be equal to 78, beyond which light is entirely attenuated, as evidenced by the radiative intensity. This value drops to 64 near the end of the CCW, which also matches the transmission signal through the device at the corresponding frequency. It can therefore be inferred through interpolation of the radiative intensity that for an 800-cavity CCW, the 1/e amplitude decay length is  $\approx 378 \mu\text{m}$  for  $n_g \approx 61$  near the high-frequency edge of the band. It should be noted that this value depends considerably on the radiative losses of the CCW, which is evidenced by the lower  $n_g$  cutoff near the low-frequency edge of the band, due to the greater intrinsic

radiation in that range. Nevertheless, it provides an order of magnitude estimate with respect to the current fabrication disorder figure in CCWs.

In conclusion, we have experimentally investigated slow light properties in CCWs featuring a large group index-bandwidth product, comprising up to 800 cavities. By reconstructing the dispersion response through Fourier-space imaging, slow light properties were elucidated across the dispersion band. The impact of finite-size effects was evident, as observed with the convergence of the CCW dispersion toward periodic-boundary conditions in longer cavity chains. A partial contraction of the operational bandwidth and degradation of transmission were found in longer devices. Disorder was shown to limit device performance for cavity chain lengths approaching 800 cavities. The magnitude of transmission fluctuations and scattering losses scaled with the number of coupled cavities, as the device size became comparable to the localization length of the CCW mode. The measured performance figures however are specific to the degree of disorder and radiative losses for the implemented CCW design. Improved performance in extended cavity chains may be attained with future advances in fabrication, namely, by achieving large-scale uniformity with near atomic-scale patterning accuracy such as to minimize residual disorder. Furthermore, the exploration of waveguide designs featuring topological protection is a promising avenue for slow light that is more robust to disorder.

## METHODS

**Fabrication.** ZEP-520A resist (positive-tone) was spun on a Si-on-insulator wafer (Si thickness = 220 nm), and the layer was subsequently patterned by electron-beam lithography using a 100 keV beam. After resist development, inductively coupled plasma etching of the Si layer was conducted using fluorine-based chemistry to transfer the mask pattern. SU8 spot-size converters were then patterned using UV photolithography, guided by predeposited alignment markers. The

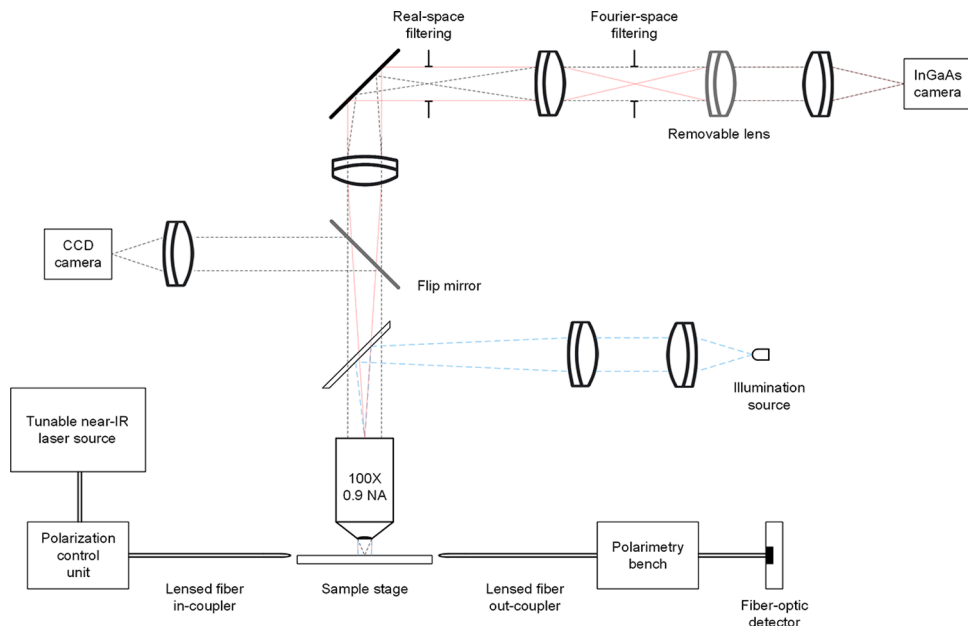


**Figure 8.** Schematic illustration of the experimental Fourier-space imaging setup.

PhC membrane was finally released by buffered-HF etching of  $\text{SiO}_2$ , after protecting the SU8 waveguides with photoresist.

**Fourier-Space Imaging.** An imaging microscopy setup featuring an end-fire excitation and collection configuration was utilized for the characterization of the CCW devices. A schematic of the experimental setup is displayed in Figure 8. The sample is placed at the focal plane of a high numerical aperture objective (Leica 100 $\times$ , NA = 0.9), and an identical pair of lensed optical fibers is used for excitation and collection at the sample facets. Spatial filtering is applied at the conjugate image plane to select the region-of-interest out of the field-of-view and to suppress undesirable stray scattering. The spatially filtered acquisition region is  $25 \times 25 \mu\text{m}^2$ , enclosing approximately 36 cavities. This is the smallest tolerated area to avoid degrading the k-space resolution beyond  $0.05 \mu\text{m}^{-1}$  (specific to the employed optics and acquisition near  $\lambda = 1550 \text{ nm}$ ).

This frequency-domain characterization technique relies on collecting out-of-plane emission from coupled PhC cavities. The emission relates to the wave vector of the supported propagating CCW mode through momentum conservation at the Si-air interface. By measuring the far-field radiative angle for a given wave vector  $k$ , the in-plane Bloch wave vector of the mode is determined. The dispersion relation is then reconstructed by scanning the input laser wavelength and accumulating the far-field patterns.

Dispersion data points are obtained through frequency weighing of the radiative intensity on the discretized k-axis. The experimental accuracy of wavelength and momentum correspond to  $\sigma_\lambda = 3 \text{ pm}$  and  $\sigma_k = 0.025 \mu\text{m}^{-1}$ . For the extraction of slow light properties, a tight-binding fit is applied to the dispersion data points. A nonlinear curve-fitting procedure is implemented utilizing orthogonal distance regression to account for the experimental error. The accuracy of the fitting parameters, e.g. first-neighbor coupling strength, is obtained from the confidence intervals, whose bounds we specify at 95%.

## ■ AUTHOR INFORMATION

### Corresponding Author

\*E-mail: [mohamedsabry.mohamed@alumni.epfl.ch](mailto:mohamedsabry.mohamed@alumni.epfl.ch).

### ORCID

Mohamed Sabry Mohamed: [0000-0002-4162-4122](https://orcid.org/0000-0002-4162-4122)

### Notes

The authors declare no competing financial interest.

## ■ ACKNOWLEDGMENTS

The authors would like to acknowledge financial support from the Swiss National Science Foundation, through project number 2000020\_169560, as well as fruitful discussions with Juan Vasco. Y.L. and A.B. acknowledge funding from the Natural Sciences and Engineering Research Council of Canada (NSERC) Discovery Grant RGPIN-2017-06859.

## ■ REFERENCES

- (1) Vlasov, Y. A.; O'Boyle, M.; Hamann, H. F.; McNab, S. J. Active control of slow light on a chip with photonic crystal waveguides. *Nature* **2005**, *438* (7064), 65–69.
- (2) Shi, Z.; Boyd, R. W. Slow-Light Fourier Transform Interferometer. *Phys. Rev. Lett.* **2007**, *99* (24), 240801.
- (3) Xiong, C.; et al. Slow-light enhanced correlated photon pair generation in a silicon photonic crystal waveguide. *Opt. Lett.* **2011**, *36* (17), 3413.
- (4) Matsuda, N.; Takesue, H.; Shimizu, K.; Tokura, Y.; Kuramochi, E.; Notomi, M. Slow light enhanced correlated photon pair generation in photonic-crystal coupled-resonator optical waveguides. *Opt. Express* **2013**, *21* (7), 8596.
- (5) Takesue, H.; Matsuda, N.; Kuramochi, E.; Munro, W. J.; Notomi, M. An on-chip coupled resonator optical waveguide single-photon buffer. *Nat. Commun.* **2013**, *4*, 1–7.
- (6) Notomi, M.; Kuramochi, E.; Tanabe, T. Large-scale arrays of ultrahigh-Q coupled nanocavities. *Nat. Photonics* **2008**, *2* (12), 741–747.
- (7) Matsuda, N.; Kuramochi, E.; Takesue, H.; Notomi, M. Dispersion and light transport characteristics of large-scale photonic-crystal coupled nanocavity arrays. *Opt. Lett.* **2014**, *39* (8), 2290.

- (8) Lai, Y.; Mohamed, M. S.; Gao, B.; Minkov, M.; Boyd, R. W.; Savona, V.; Houdré, R.; Badolato, A. Ultra-wide-band structural slow light. *Sci. Rep.* **2018**, *8*, No. 14811, arXiv: 1706.09625 .
- (9) Kuramochi, E.; Matsuda, N.; Nozaki, K.; Park, A. H. K.; Takesue, H.; Notomi, M. Wideband slow short-pulse propagation in one-thousand slantingly coupled L3 photonic crystal nanocavities. *Opt. Express* **2018**, *26* (8), 9552.
- (10) Minkov, M.; Savona, V. Wide-band slow light in compact photonic crystal coupled-cavity waveguides. *Optica* **2015**, *2* (7), 631–634.
- (11) Schulz, S. A.; O’Faolain, L.; Beggs, D. M.; White, T. P.; Melloni, A.; Krauss, T. F. Dispersion engineered slow light in photonic crystals: a comparison. *J. Opt.* **2010**, *12*, 104004.
- (12) Sumetsky, M.; Eggleton, B. Modeling and optimization of complex photonic resonant cavity circuits. *Opt. Express* **2003**, *11* (4), 381–391.
- (13) Iwase, E.; et al. Control of buckling in large micromembranes using engineered support structures. *J. Micromech. Microeng.* **2012**, *22* (6), No. 065028.
- (14) Le Thomas, N.; Houdré, R.; Kotlyar, M. V.; O’Brien, D.; Krauss, T. F. Exploring light propagating in photonic crystals with Fourier optics. *J. Opt. Soc. Am. B* **2007**, *24* (12), 2964.
- (15) Caselli, N.; et al. Tailoring the Photon Hopping by Nearest-Neighbor and Next-Nearest-Neighbor Interaction in Photonic Arrays. *ACS Photonics* **2015**, *2* (5), 565–571.
- (16) Le Thomas, N.; Zabelin, V.; Houdré, R.; Kotlyar, M. V.; Krauss, T. F. Influence of residual disorder on the anticrossing of Bloch modes probed in  $k$  space. *Phys. Rev. B: Condens. Matter Mater. Phys.* **2008**, *78* (12), 125301.
- (17) Mazoyer, S.; et al. Statistical fluctuations of transmission in slow light photonic-crystal waveguides. *Opt. Express* **2010**, *18* (14), 14654–14663.
- (18) Lai, Y.; et al. Genetically designed L3 photonic crystal nanocavities with measured quality factor exceeding one million. *Appl. Phys. Lett.* **2014**, *104* (24), 241101.
- (19) Vasco, J. P.; Savona, V. Disorder effects on the coupling strength of coupled photonic crystal slab cavities. *New J. Phys.* **2018**, *20*, No. 075002, arXiv: 1805.03012 .
- (20) Kramer, B.; MacKinnon, A. Localization: theory and experiment. *Rep. Prog. Phys.* **1993**, *56* (12), 1469–1564.
- (21) Aoki, H. Critical behavior of extended states in disordered systems. *J. Phys. C: Solid State Phys.* **1983**, *16* (6), L205.
- (22) Hughes, S.; Ramunno, L.; Young, J. F.; Sipe, J. E. Extrinsic optical scattering loss in photonic crystal waveguides: Role of fabrication disorder and photon group velocity. *Phys. Rev. Lett.* **2005**, *94* (3), 1–4.
- (23) Mazoyer, S.; Hugonin, J. P.; Lalanne, P. Disorder-induced multiple scattering in photonic-crystal waveguides. *Phys. Rev. Lett.* **2009**, *103* (6), 1–4.